Composites Science and Technology 162 (2018) 146–155

Contents lists available at ScienceDirect

Composites Science and Technology

journal homepage: www.elsevier.com/locate/compscitech

Identifying interphase properties in polymer nanocomposites using adaptive optimization

Yixing Wang[a], Yichi Zhang[a], He Zhao[a], Xiaolin Li[c], Yanhui Huang[d], Linda S. Schadler[d], Wei Chen[a], L. Catherine Brinson[a,b,*,1]

[a] Department of Mechanical Engineering, McCormick School of Engineering and Applied Science, Northwestern University, 2145 Sheridan Road, Evanston, IL 60208, USA
[b] Department of Material Science and Engineering, Northwestern University, 2220 Campus Drive, Evanston, IL 60208, USA
[c] Theoretical and Applied Mechanics Program, Northwestern University, 2145 Sheridan Road, Evanston, IL 60208, USA
[d] Department of Material Science and Engineering, Rensselaer Polytechnic Institute, 110 8thStreet, Troy, NY 12180, USA

ARTICLE INFO

Keywords:
A: Nanocomposites
B: Interphase
C: Finite element analysis (FEA)
C: Adaptive optimization

ABSTRACT

To predict the properties of nanocomposites, computational models have demonstrated that the interphase behavior can be expressed using the matrix properties with a modified (shifted) frequency. The amount of the shift necessary for a given sample data set can be determined by achieving the best fit between the predicted curve from a computation model and the experimental data through trial-and-error. However, with the complexity of experimental data and expensive computational costs, a manual process to solve this inverse problem is impractical to handle many experimental data sets. This difficulty hinders investigation of the underlying principles behind nanocomposite interphase. In this work, we present an adaptive optimization approach that accelerates the search for interphase properties in polymer nanocomposite data sets by solving the inverse problem using global optimization. The objective is to minimize the difference between the predicted bulk property of a nanocomposite with that from the experiment data. A Gaussian Process (GP) model is built as a surrogate of the objective function with quantification of prediction uncertainty. An adaptive sampling strategy is applied to effectively navigate the complex search space by iteratively selecting the next sampling point based on an expected improvement function. The surrogate model and the optimal solution evolve until the desired objective is achieved. The approach is tested on both the simulations of dielectric and viscoelastic properties in nanocomposites. Our work provides insight into identifying the interphase properties for polymer nanocomposites using adaptive optimization and demonstrates the potential of data-driven approach for achieving a deeper understanding of the interphase properties and its origins.

1. Introduction

Polymer nanocomposites have attracted great interest in recent years because of their potential as tailored materials with enhanced properties [1–3]. Recent experiments have shown that polymer nanocomposites are able to achieve significant improvement in dielectrical, thermal, mechanical and other physical properties compared with their parent polymer systems [4–9]. More importantly, these outstanding properties can be achieved at low filler loadings such that the polymer system does not sacrifice the advantages of easy processability [10,11].

One of the reasons for the enhancement in properties is the large interphase region that results from both the strong chemical and geometric interactions between the particle surface and the polymer segments near the particle and the high surface-to-volume ratio of the nanoinclusions. For example, if a composite sample contains 5 wt% of 40 nm particles perfectly dispersed, the resulting total interfacial surface area is about $3.5 m^2/cm^3$. As illustrated in Fig. 1, due to the interacting cooperative nature of the macromolecular network, the interphase area extends beyond the layer of matrix chains directly bound to the filler surface resulting in the significant extension of the interphase domain into the matrix [12].

In order to understand the behavior of the interphase and make accurate predictions of nanocomposite properties, efforts have been made to measure the interphase thickness and its mechanical or dielectric response [13–16]. Although direct measurements of the interphase are limited because of challenges in experimental visualization at

* Corresponding author. Department of Mechanical Engineering, McCormick School of Engineering and Applied Science, Northwestern University, 2145 Sheridan Road, Evanston, IL 60208, USA.
E-mail address: cbrinson@northwestern.edu (L.C. Brinson).
[1] Dr. Brinson is currently Professor of Mechanical Engineering and Materials Science at Duke University, Durham NC, USA.

https://doi.org/10.1016/j.compscitech.2018.04.017
Received 12 September 2017; Received in revised form 14 March 2018; Accepted 11 April 2018
Available online 28 April 2018
0266-3538/

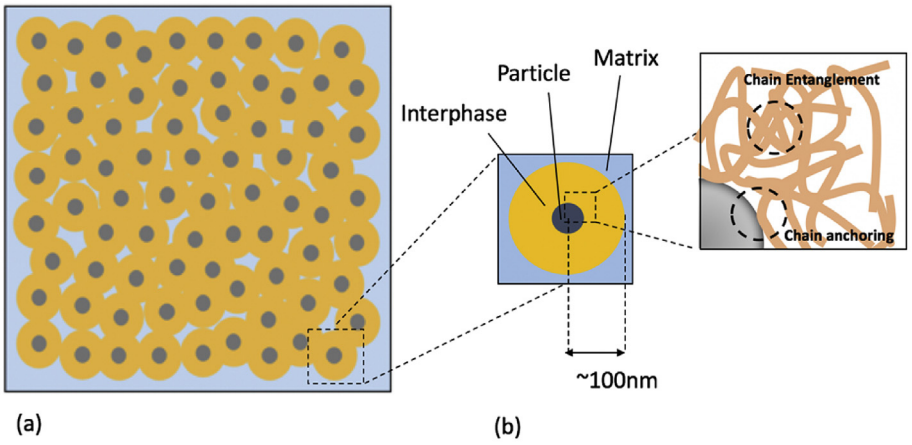

Fig. 1. Interphase configuration. (a) Schematic of the interphase regime in a nanocomposite sample. (b) Schematic showing the extended interphase structure. Yellow chains directly anchored to or chemically interacting with nanofiller. Blue chains impacted by filler indirectly through interaction with yellow chains. Cooperatively interacting chains propagate interphase zone to persist to the order of 100 nm from the particle surface. Note: figures not to scale.

the nanoscale, recent studies focus on measuring the local elastic and viscoelastic properties in different polymer microdomains by correlating thin film and nanocomposite data, providing adequate evidence that the local polymer properties are significantly altered in the vicinity of polymer surface [17–22]. The actual thickness of the interphase may vary depending on specific polymer-filler system and has a wide range values from several nanometers to hundreds of nanometers. In particular, an atomic force microscopy (AFM) -based method that directly measures the mechanical properties of polymers adjacent to a substrate with nanometer resolution shows a gradient of mechanical properties extending approximately 100 nm from confining surfaces [20,23].

To predict properties of nanocomposites, continuum mechanics methods are often employed in which three phases must be considered: polymer, particle and interphase. Micromechanical models [24], such as Halpin-Tsai, Mori-Tanaka and the self-consistent scheme have been applied to predict the thermomechanical behavior of nanocomposites [25–28]. A variety of analytical models have been developed to analyze the dielectric behaviors including the Bruggeman model [29], Lichtenecker model [30] and Todd-Shi model [31]. Given experimental limitations to measure interphase properties directly, one approach to determine the interphase properties is inversely through tuning the parameters in finite element analysis or micro-scale model constitutive equations using the bulk composite properties from experiments [31–34]. Importantly, in order to capture the dispersion state or the morphology information of the fillers, multiscale simulations are often necessary. For example, multiscale approaches have been applied to study the viscoelastic properties in polymer nanocomposites [35–37].

FEA simulations can accommodate complicated non-homogeneous material systems with explicit configuration of all relevant material phases. This makes FEA a good option for to analyze behavior of nanocomposites and include both important nanofiller dispersion as well as interphase properties. We have developed finite element models for analyzing the thermal and mechanical [32,38–40] and dielectric behavior [33,41] of polymer nanocomposites and investigated the impact of the interphase on the corresponding properties. We have shown that in some cases, the interphase properties can be described by shifting factors based on the pure matrix properties, which can be well represented by the Prony Series as a parametric expression of multiple relaxation times and strengths [38,41]. Given experimental data for both the pure matrix and bulk nanocomposites properties (either dielectric or thermomechanical) the necessary interphase properties can be determined from a trial-and-error based iterative tuning procedure by matching simulated results from FEA with experimental data. However, there are several disadvantages for this trial-and-error based manual fitting. First, this process can be very time-consuming given the complexity of experimental data and computational cost of the FEA (a single FEA model for one sample with ~10 k elements requires 30 min to run on typical server). Since many manual iterations are often required, where the optimal shifting factors are guessed based on the previous outputs, this tedious manual tuning process prohibits efficient investigation of the correlation between shifting factors and material constituent characteristics.

In this work, we present a combined FEA and optimization approach to accelerate the search of optimal interphase properties given experimental data of bulk property for the composite. Our objective is to find the optimal interphase properties that minimize the difference between simulations and experiments, and to do so with an automated procedure. We adopt an adaptive global optimization approach that incorporates Gaussian Processing (GP) modeling [42,43] and sequential sampling strategy [44] to efficiently find the global optimal solution. Our proposed method can accurately find the optimal shifting factors given experimental data in tens of iterations, which significantly eases the computation costs from simulations. We demonstrate our method by finding both dielectric and mechanical properties of the interphase based on composite property data. This method is an efficient and reliable tool to determine interphase properties and can facilitate future work of uncovering the relationship between interphase properties and material constituents.

2. Methodology

Our goal is an optimization of interphase properties for a single sample, for which we have a) constituent properties, b) composite properties, c) microstructure information. We seek to determine the interphase properties that will yield the composite properties (b) from (a) and (c). We assume the interphase properties can be represented by shift factors with respect to matrix properties (defined in more detail below). Thus, we seek to find the shift factors that will optimally match the composite data via an automated procedure applying adaptive optimization. Based on experience and literature data we begin with reasonable bounds for the shift factor values, and the space defined by the n-dimensional factors (n = 5 for dielectric case [41], n = 2 for mechanical case [36]) varying in these bounds defines the search space for the adaptive optimizer. The key components of the adaptive optimization method are summarized in Fig. 2: (1) The empirical bounds of shift factors are used to set the range to sample initial training sets of shift factors from design of experiments (DOE) using Optimal Latin hypercube (OLHC). For each set of shifting factors, the FEA model is run and outputs the simulated result. Then the objective function is formulated as the difference between the experimental data and the simulation using mean square error (MSE); (2) A surrogate model, in our case, a Gaussian Process (GP) model, uses the training data to learn the relationship between the objective (Difference F) and features (shifting factors), with uncertainties.; (3) adaptive optimization (selector) provides the most promising candidate points for the new simulation and augments the initial shift factor set from DOE. In our study, new

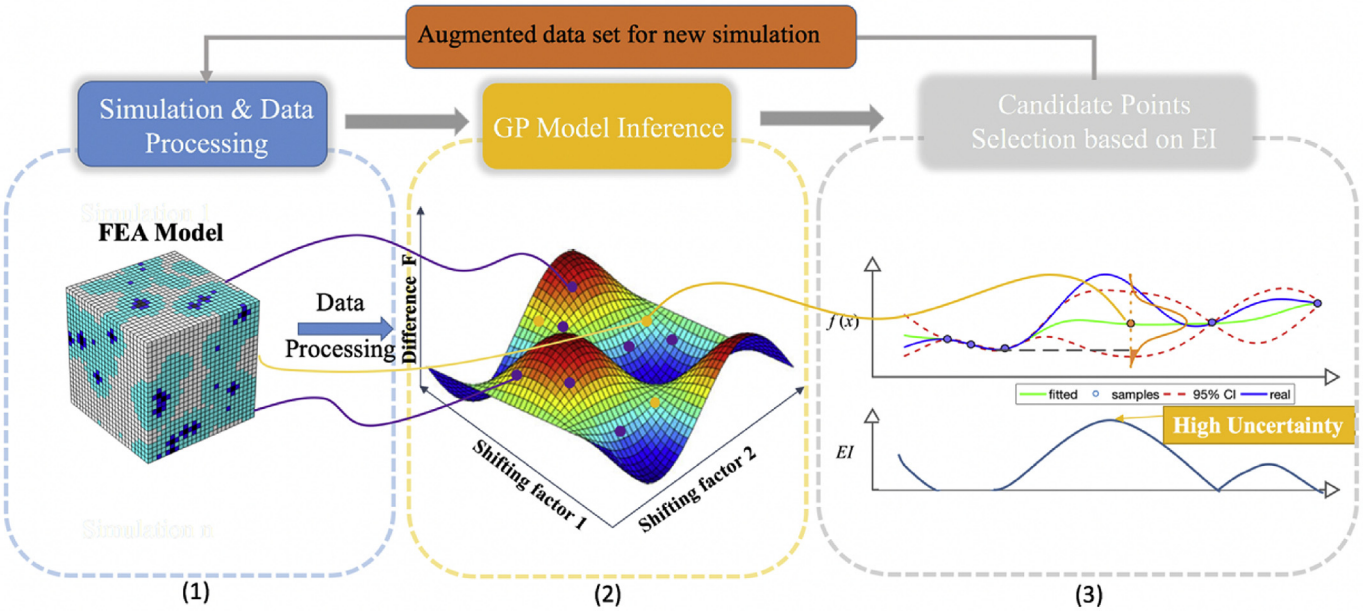

Fig. 2. Our automated adaptive optimization strategy for searching the interphase properties: (1) FEA is run on each point in the initial shift factor set from DOE and then processed to formulated our objective function by calculating the difference between simulated results and experiments using MSE. (2) A GP model is applied to construct the surrogates for predicting the value of objective function (Difference F) within the design space. The purple points are initial sampling points from DOE and the yellow points are sequentially generated by EI in (3). (3) EI chooses the best candidate points for additional simulation. The new candidate points augment the initial training shift factor set from DOE to further improve the surrogate model and prediction accuracy.

candidate points are selected based on the feedback from the surrogate model at a previous step by calculating the Expected Improvement (EI). Step (2) and (3) is usually identified as an adaptive optimizer, which augments the initial training shift factor set and drives the subsequent iterative improvement of the surrogate model and prediction accuracy.

2.1. Interphase FE model

Our method is developed and tested on two cases for polymer nanocomposite response data: viscoelastic simulations and dielectric simulations. For both cases, we have developed finite element models to simulate the composite properties given the microstructure from Scanning Electron Microscope (SEM) or Transmission electron microscopy (TEM) images [33,38]. The schematic of the FEA model for dielectric studies and viscoelastic simulations is similar except different software is used to run the simulations (*COMSOL* for dielectric and *ABAQUS* for viscoelastic simulations). The FEA configuration is shown in Fig. 3. The microstructure dispersion information is directly obtained from TEM micrograph images (Fig. 3a). Then a binary image showing filler and matrix phases is generated by application of a previously developed Niblack analysis algorithm [45]. The binary image is then characterized to identify the geometric descriptors and reconstruct the equivalent 3D microstructure and assign each point to a material constituent in the FEA model (filler, interphase, matrix) (Fig. 3c).

The geometric information of the filler and matrix can be directly obtained from the original image, while the interphase regime between the filler and particle is assumed to be represented by an extended layer around each particle. Thickness of the interphase is reasonably assumed to be 50 nm in our study based on previous studies on filler-filler spacing and experiment measurements [20,46]. The FEA model is then run in the respective software to obtain the frequency-dependent viscoelastic or dielectric response.

These interphase FEA models have been used with a manual inverse approach to determine interphase properties [36,38,41]. In these studies, the shift factors to relate interphase properties to matrix properties are defined differently for each property case. In viscoelastic simulations, a broadening factor B and frequency-shifting factor S are applied to describe the interphase behavior based on the matrix property. B accounts for the broadening effect of the loss peak while S accounts for the horizontal shift of relaxation times in the frequency domain (Fig. 4a). To describe the dielectric interphase, due to the multiple relaxations observed in the pure matrix, the alpha and beta relaxations are modeled separately and a five-dimensional shifting factor set is applied in the interphase model. The threshold value of the relaxation time is determined based on experimental data ($\tau_0 = 0.01$ in our case) so that the corresponding threshold frequency separates the relaxation

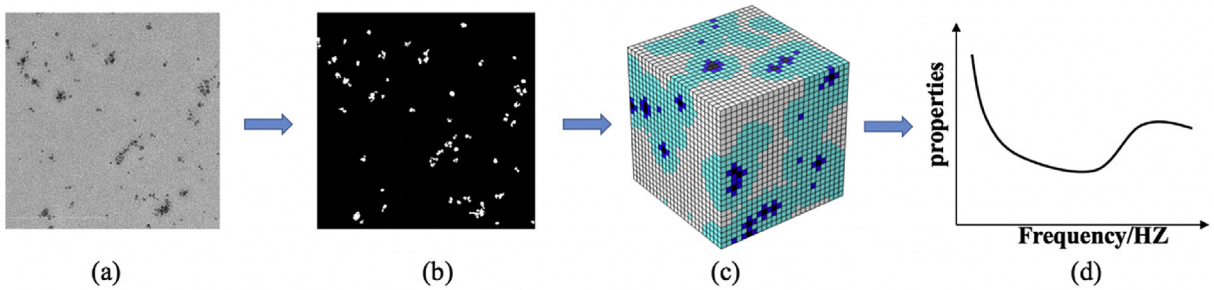

Fig. 3. Configuration of FEA model in COMSOL (dielectric simulation) and ABAQUS (viscoelastic simulation). a) Sample TEM image, b) binary image of matrix and filler phases, c) reconstructed microstructure, d) frequency dependent dielectric properties or viscoelastic response predicted from simulation.

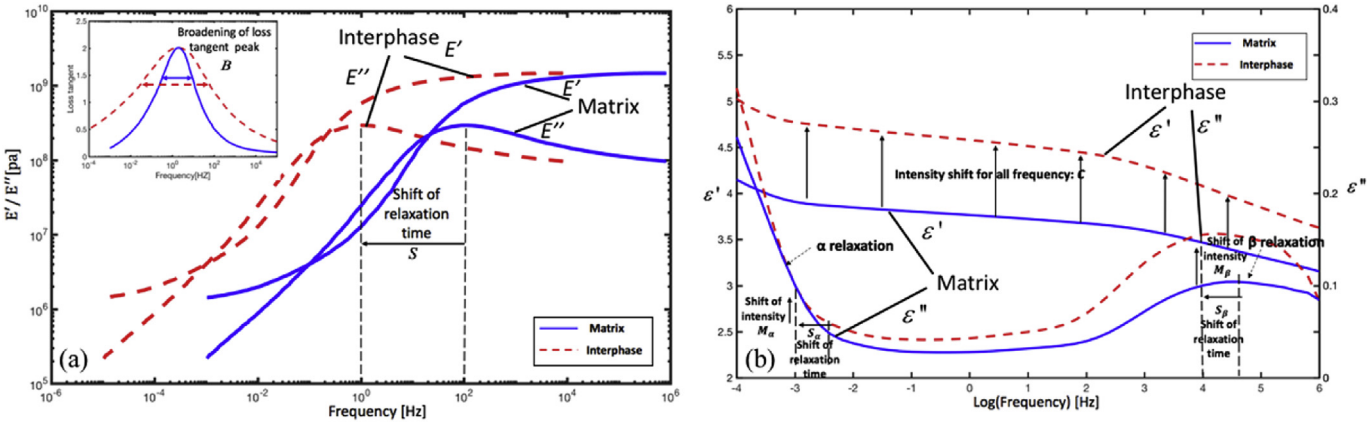

Fig. 4. Relation of material properties between the interphase and pure matrix represented by shifting factors in frequency space for (a) viscoelastic interphase properties with $S = 2$, $B = 2$ (b) dielectric interphase properties with $s_\alpha = 2$, $M_\alpha = 1.5$, $S_\beta = 2$, $M_\beta = 1.5$, $C = 0.5$.

peak into low (α relxation) and high frequency regions (β relxation). For each relaxation (alpha or beta relaxation), two shifting factors (M_α and S_α for alpha relaxation; M_β and S_β for beta relaxation) are applied to account for the change of intensity (M_α and M_β) and the shift of relaxation times (S_α and S_β) for respective relaxations. An additional constant, C, describes the intensity shift of ε' (Fig. 4b).

2.2. Optimization objective

The objective of this work is the development of a rigorous automated method to predict the optimal interphase shifting factor set which enables a simulation result to best fit with the experimental data, thus determining the interphase properties is an inverse problem. There are a number of choices of mathematical measures that quantify the discrepancy between simulation and experimental results. These measures can be divided into three categories: magnitude-phase-comprehensive metrics, single-value metrics, and analysis of variance metrics. We tested the performance of different metrics on characterizing the difference between simulation and experimental results and found that the mean square error (MSE) is the best descriptor for our problem in terms of the final prediction accuracy. The MSE of the predictor in our study can be expressed as,

$$MSE = \frac{1}{m}\sum_{i=1}^{m}(c_i - e_i)^2 \tag{1}$$

where c_i and e_i represent each simulated data point in frequency and experimental data point in frequency respectively.

In order to search for the optimal shifting factors, a proper target function needs to be defined. Ideally, the optimal shift factors should lead to well-matched data curves between FEA and experimental results. Equivalently, the minimal discrepancy between simulated and experimental data across the entire frequency band is desired. Additionally, for our case, it is required to minimize the difference from both real and imaginary property data simultaneously, which leads to a multi-objective optimization problem. To addresses this problem, we first characterize the difference from the real and imaginary parts separately using Equation (1) for every shift factors set across the OLHC space (initially generated from DOE) and obtain the vector of real part difference $\mathbf{f}^1$ and imaginary part difference $\mathbf{f}^2$ for each data point in the OLHC space.

To develop the multi-objective approach, for every shift factors set across the OLHC space we normalize the objective function as follows:

$$\mathbf{f^{i.norm}} = \frac{\mathbf{f^i} - \mathbf{f^i_{min}}}{\mathbf{f^i_{max}} - \mathbf{f^i_{min}}} \tag{2}$$

Here, $\mathbf{f^i}$ represents the vector of difference calculated from MSE for real (i = 1) or imaginary part (i = 2), $\mathbf{f}^i_{\min}$ and $\mathbf{f^i_{max}}$ represent the minimum and maximum difference value for the entire design space respectively. So from this equation, we are able to generate two normalized difference vectors for the real ($\mathbf{f^{1.norm}}$) and imaginary properties ($\mathbf{f^{2.norm}}$) separately. Then, we formulate this multi-objective function as the summation of weighted difference of the real and imaginary components:

$$\mathbf{F} = w_1 \cdot \mathbf{f^{1.norm}} + w_2 \cdot \mathbf{f^{2.norm}} \tag{3}$$

Here, w_1 and w_2 are the weight of real and imaginary components. $\mathbf{f^{1.norm}}$ and $\mathbf{f^{2.norm}}$ are normalized error vector from real and imaginary components, respectively. $\mathbf{F}$ is the final vector form of the objective describing the difference between the simulated data and the experimental results. Using $\mathbf{F}$ as the objective function and shifting factors as features, the next step is to build up surrogate models and make predictions.

Considering the relatively high cost of simulation models, direct optimization that requires a large number of iterations is usually infeasible. An adaptive optimizer [47] has been developed to address such challenges: it combines surrogate modeling [42] and infill criterion [48] to refine the prediction adaptively while minimizing the sampling cost. Such adaptive strategy has been applied to sequentially optimize and design new materials with target properties [49–51]. Through detailed derivations in Supporting information, an adaptive optimizer is applied to construct the surrogate model and suggest the next optimal sampling points in order to minimize the objective function and return the optimal solution iteratively.

3. Results and discussion

In this section, a representative dielectric data set (for a nanocomposite composed of 2 wt% bimodal anthracene-PGMA grafted silica in epoxy [33,52]) is first selected to develop and test our methods. Detailed intermediate results are given to illustrate the methodology. Later, this algorithm is further tested on viscoelastic studies with the experiment samples collected from nanocomposite samples composed of 2 wt% Chloro-modified nanosilica in Polystyrene (PS) nanocomposites [53]. Detailed experimental information on measurement of dielectric and viscoelastic responses can be found in the supporting information. We have TEM images and reconstructed microstructures for both the viscoelastic and dielectric samples as shown in Fig. 5. Note that the microstructures are statistically equivalent to the actual samples and are created using an algorithm developed earlier [54].

In our previous work [41], we determined manually fitted shift factors for a number of dielectric nanocomposites and using this prior study, we can select reasonable ranges within which the shift factors may vary (Table 1).

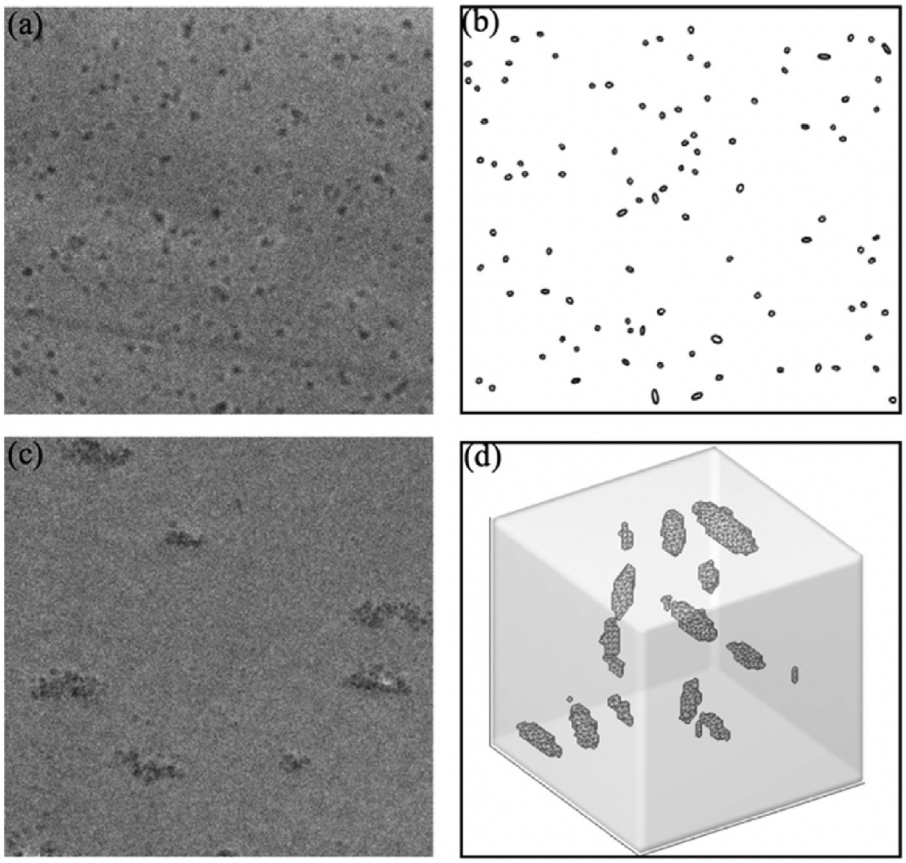

Fig. 5. TEM images and the reconstructed microstructure used in FEA. (a) 2 wt% bimodal anthracene-PGMA grafted silica in epoxy TEM image, (b) reconstructed 2D microstructure of (a), (c) 2 wt% Chloro-modified nanosilica in PS TEM image, (d) reconstructed 3D microstructure of (c).

Table 1
Dielectric shifting factor design space.

Shifting factor	S_β	M_β	S_α	M_α	c
Range	0.4–1	1.5–3	0–0.2	0.7–2	0.3–2.5

For this dielectric study, 20 sets of shifting factors are generated as the initial data set within the empirical ranges through design of experiments (DOE) created by applying the optimal Latin hyper cube (OLHC) sampling technique [55]. The sample points are selected to cover the entire input variable space bounded by the given ranges (the blue points in Fig. 7b–d illustrate the initial DOE for this example). Given the microstructure obtained from the TEM image for the chosen sample (Fig. 5a and b), FEA simulations are performed over the 20 OLHC samples for shift factors to obtain the composite dielectrical response. The FEA model generates two outputs on each simulated sample: frequency-dependent storage and loss dielectric (or

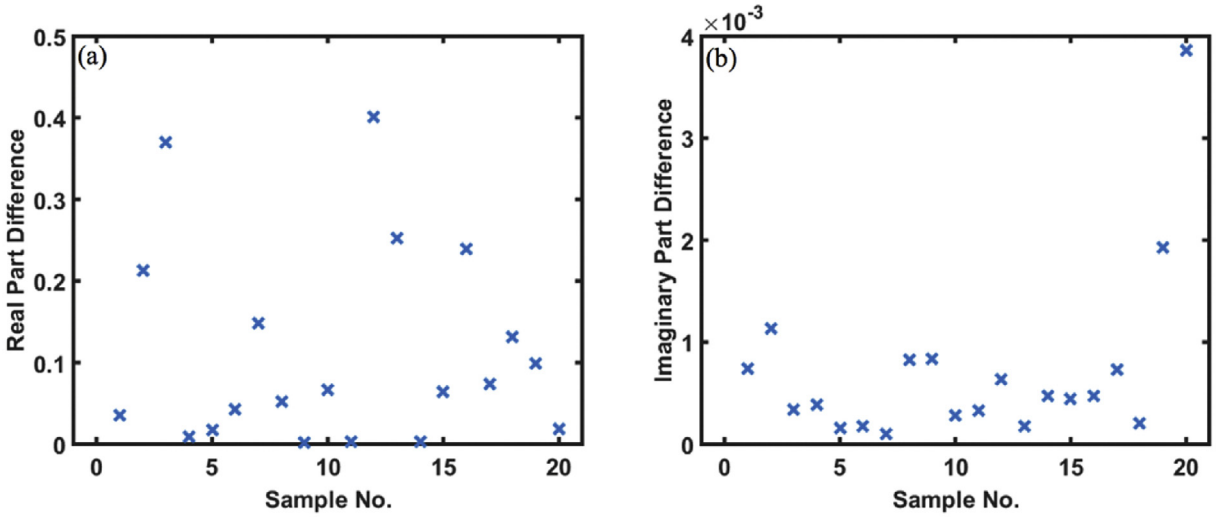

Fig. 6. Differences between 20 DOE designed simulations and experiment data as applied to 2 wt% bimodal anthracene-PGMA grafted silica in epoxy sample. (a) Real part difference characterized by MSE; (b) Imaginary part difference characterized by MSE.

viscoelastic) curves. These results are then processed by calculating the difference between the simulated curves and the target experimental data using Equation (1). For the chosen dielectric data set, the real and imaginary differences, $\mathbf{f}^1$ and $\mathbf{f}^2$, characterized for the initial 20 shifting factor sets are plotted in Fig. 6.

It can be seen that the difference calculated from two parts have significantly different orders of magnitudes, which makes direct comparison difficult. Therefore, it is necessary to normalize the magnitudes using Equation (2) and formulate a multi-objective optimization problem applying Equation (3) such that minimizing the difference from both real and imaginary data simultaneously can be achieved. Below, an adaptive optimizer is applied to navigate the high dimensional design space and make accurate predictions.

In our study, our objective is to minimize the difference, for which the ideally optimal value of 0 indicates a perfect match between the simulated and experimental results. Practically, we find a threshold value C, indicating an acceptable fit between the experimental data and simulated results. By applying an adaptive optimizer, at each iteration, a new sampling point is given based on the feedback from the optimization to augment the training set and the iteration will cease after the output difference is less than the threshold:

$$\min(F_{\mathbf{k}+1}) \leq C, \tag{4}$$

where $F_{\mathbf{k}+1}$ represents the surrogate model at k + 1 step. The threshold C may vary from case to case while the C is set to 0.01 in our study. Additionally, to avoid infinite loop of the adaptive optimizer arising from bad data or parameter limits, the loop is set to terminate after this is no sign of decreasing difference after 20 iterations.

In order to evaluate the prediction accuracy of the surrogate model at each iteration, a separate validation set with sample size 30 is generated by random sampling another 30-shifting factor sets within the design space and running simulations accordingly. Then the difference between the simulations and the experiment for the validation set can be evaluated using Equation (3). The surrogate model error at each step is then evaluated by calculating the mean square error between the predicted difference from the surrogate model with that from the validation set. Fig. 7 shows the evolution of the surrogate model accuracy as iteration progresses in the adaptive optimization process.

In order to visualize the sample distribution during the optimization process, we choose two factors (S_α and S_β) and plot the distribution on iteration 2, 17, and 23 respectively (Fig. 7 b,c,d). On iteration 1, only the initial 20 training points from OLHC (blue points in the Fig. 7b) are used to make predictions. Then later, at each step, a new sampling point (red in Fig. 7b) is added based on the maximum EI criterion. The newly added points are concentrated on the boundaries and the space with coarse initial sampling showing that the adaptive optimizer is able to automatically explore the entire design space with high uncertainties rather than search only in a local space which could result in a local minimum. It is noted that the error for each step keeps decreasing (though not monotonically, likely due to the model uncertainties) indicating an increase in model accuracy as new sampling points are added. Additionally, the dropping EI in the model also suggests the decreasing uncertainty of the surrogate models and the increasing model accuracy with the identified shift factors.

Fig. 8 shows how our predicted optimal solution behaves as a function of iterations. The prediction accuracy at each step is evaluated by calculating the discrepancy between the simulated data using the predicted shifting factor from the adaptive optimizer and the given experimental properties using Equation (3). Fig. 8a shows that the prediction accuracy of $\mathbf{x}opt_{\mathbf{k}}$ at each step increases as a function of iterations. We also show the comparison between the simulated result and the experimental data on iteration 1, 12, and 20, showing that the improvement of fitting quality. Iteration 1 predicts the well at some frequency ranges, but the difference is still much greater than our threshold $C = 0.01$ (shown as dashed line in Fig. 8a). As the iteration proceeds, the decreasing difference value indicates better fitting (iteration 12) and it takes 20 iterations before the difference is less than the threshold. Ideally, the iteration stops at iteration 20 based on our stopping criteria but we plot more iterations in order to show the convergence of our adaptive optimization procedure.

Next, we want to compare different strategies including the conventional manual tuning to illustrate that the adaptive GP model can reduce the computation cost and improve searching efficiency. Using the manual fitting result as a reference, in addition to the adaptive GP model illustrated earlier, we also demonstrate the result of a one-stage GP and a random search model. The results from one-stage GP is generated by building the surrogate model based on all the sampling points in the data set and directly predict the minimal value of the objective function and the associated optimal solution at one time without sequential sampling. The result from the random search is generated by merely choosing the sample with minimal difference among all the randomly generated samples without doing any optimization. Fig. 9 shows comparisons between these different algorithms by plotting the fitted curves and the experimental data in the same figure. All the searching algorithms are compared under the same prerequisite: the simulation cost is the same (i.e. the number of performed simulations is the same, in this comparison, the number of performed simulation is set as 40). To compare the performance of each method, we also calculate the discrepancy between the simulated data using the predicted shifting factor and the given experimental properties using Equation (3) as shown in Table 2. By comparing the fitting quality, we find that the performance of the adaptive GP is at least comparable or even better compared with the manual fitting quality.

However, it is noted that the manual fitting requires guessing the optimal solution based on current fitting while the adaptive GP is able to automatically explore the design space and determine the optimal solution iteratively. Additionally, the comparison between the adaptive GP and the one-stage GP illustrates the advantages of the sequential sampling approach. The surrogate model is more accurate when determining the next sampling points 'intelligently' through calculating the EI based on the current surrogate model than sampling all the points at one time. All optimization-evolved searching algorithms tested are better than the random search. This result indicates that the prediction accuracy of the adaptive GP model is the highest comparing with other searching strategies (random searching and one-state GP) if the computation cost is required to be the same. In other words, more simulations need to be performed for other models to generate comparable result as adaptive GP. These comparisons indicate that our adaptive GP model is able to accelerate the search process while maintaining a similar accuracy compared with the manual fitting procedure.

By applying the adaptive GP model as described above, the optimal shifting factors can be determined. Since the shifting factors are descriptors for the interphase properties and completely define those properties, the interphase properties are thus determined. Fig. 10 shows the optimal interphase properties together with the matrix and composite properties. We can observe that the interphase properties are significantly different from the neat polymer matrix. This change in properties of the interphase is expected due to changes in the mobility of polymer chains near the particles which cause changes in the local physical properties such as dielectric spectra of the polymer. This interphase regime shows a higher dielectric permittivity and loss than both the matrix and composite data. This interphase property agrees with the experimental data where the addition of functional groups on fillers enhances the relative permittivity. Additionally, it is noted that the magnitude of the optimal fitted properties is dependent upon the size of the interphase regime chosen. While here we use a fixed size for the interphase zone based on prior studies on filler-filler spacing and interphase in nanodielectrics [46], the automated optimization procedure developed here can allow a thorough exploration of such variables and their impacts. Additional discussion on effect interphase thickness to the properties can be found in the supporting information.

Our adaptive GP model is also able to automatically identify the

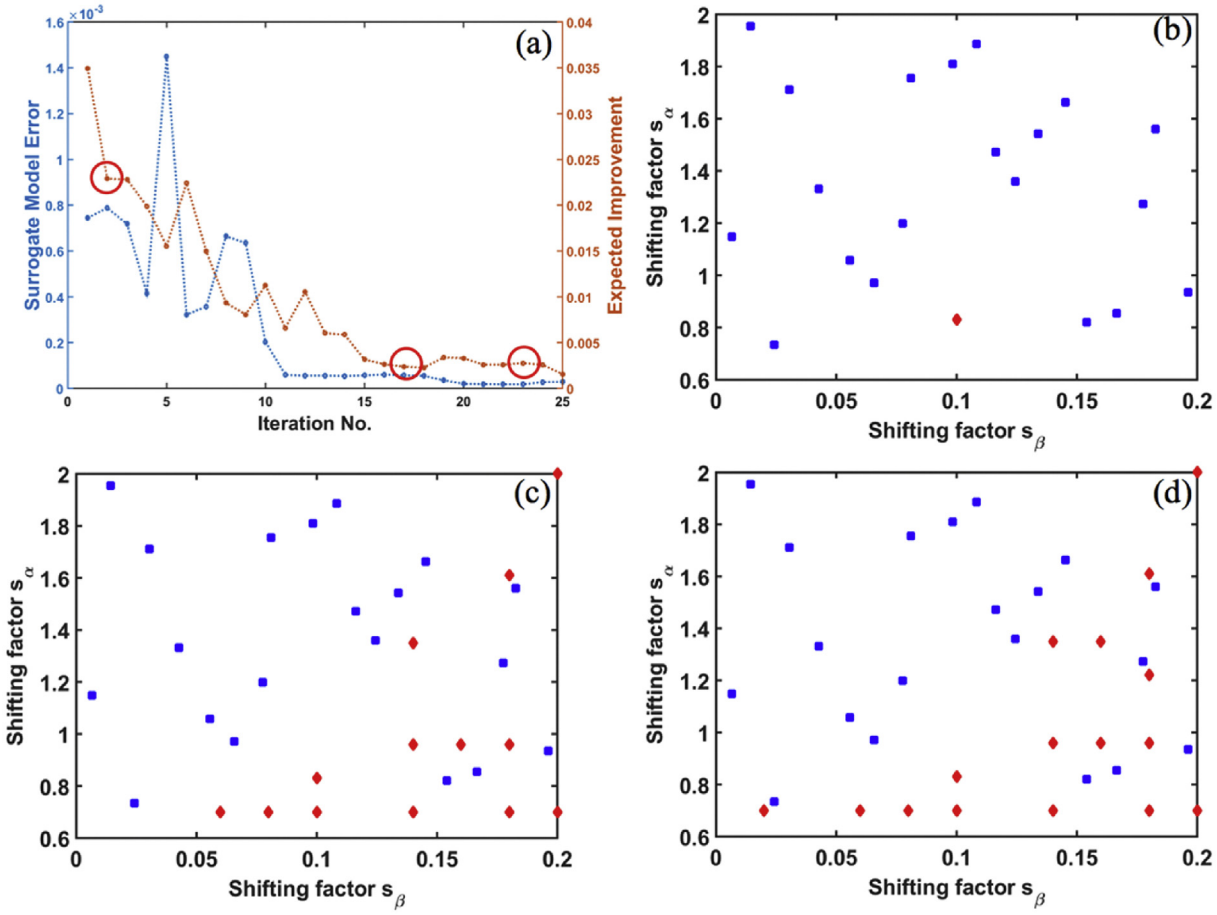

Fig. 7. Evolution of the surrogate model with successive iterations and training data distribution for 2 wt% bimodal anthracene-PGMA grafted silica in epoxy dielectric sample; (a) Surrogate model error and Maximum EI as a function of iterations, where the surrogate model error is the evaluated on a validation set with sample size 30; (b) Training sample distribution on iteration 2 (blue points are initially sampled from DOE while the red is sequentially added by Maximum EI); (c) Training sample distribution on iteration 17; (d) Training sample distribution on iteration 23.

interphase properties in viscoelastic studies. To demonstrate our method with this variation, the experimental data is taken from 2 wt% Chloro-modified nanosilica in PS [53] and we follow the same workflow as in the dielectric example. Similar to the dielectric study, the ranges of the shifting factors S and B are determined based on our understanding of physical bounds of interphase ($S \in [-2,0]$, $B \in [1,3]$) [23,38,56]. Within the empirical design space OLHC is applied to sample the initial 10 shifting factor sets and the FEA model is run based on those points. MSE is applied to characterize the difference between the simulated and the experimental data and then form our objective function and provide initial training data for the adaptive GP. Then the adaptive GP is able to explore the entire design space and make accurate predictions by sequentially adding training points based EI.

By using the strategy above, the adaptive GP model is able to automatically explore the shifting factors and obtain the simulated viscoelastic response that matches the experimental data. Fig. 11. Comparison between simulated viscoelastic response and experimental data for 2 wt% Chloro-modified nanosilica in PS shows the comparison between experimental data collected from the chosen sample and the simulated viscoelastic response based on the predicted interphase properties from adaptive GP. With the predicted interphase shifting factors from adaptive GP, simulated response is able to fit well with the experimental data. Similar to dielectric study above, the interphase properties are readily obtained directly from the optimal shifting factors. Compared with the dielectric study, it takes only three iterations for our adaptive GP model to obtain the optimal result while 20 iterations are required for the dielectric case. The two-dimensional space of the viscoelastic study allows the initial OLHC points to be nearly sufficient to build accurate surrogate models, while for the higher dimensional dielectric study, initial OLHC points is too sparse to construct accurate response surface and further iterations were required.

4. Conclusions

We have demonstrated a consistent and efficient approach for identifying the interphase properties in polymer nanocomposites by solving the inverse problem using adaptive optimization, improving prior work which was limited in accuracy and efficiency by the laborious manual iteration process. A multi-objective optimization problem is formulated through characterizing the difference from simulations and experimental data with the aim of minimizing the difference from real and imaginary parts simultaneously for frequency-dependent properties. The training data consists of shifting factor sets as optimization variables and difference as objectives. The Gaussian Process (GP) surrogate model is used to build up the relationship between the features and objectives because of its flexibility for assessing uncertainties and capability to capture nonlinear response surfaces. By choosing candidate points based on the concept of maximum expected improvement (EI) over the search space, we have shown that the surrogate model evolves and the uncertainties in the model decrease by sequentially adding points at each iteration using the EI criterion.

Using the proposed approach and given experimental data of properties and microstructure, the interphase properties on dielectric

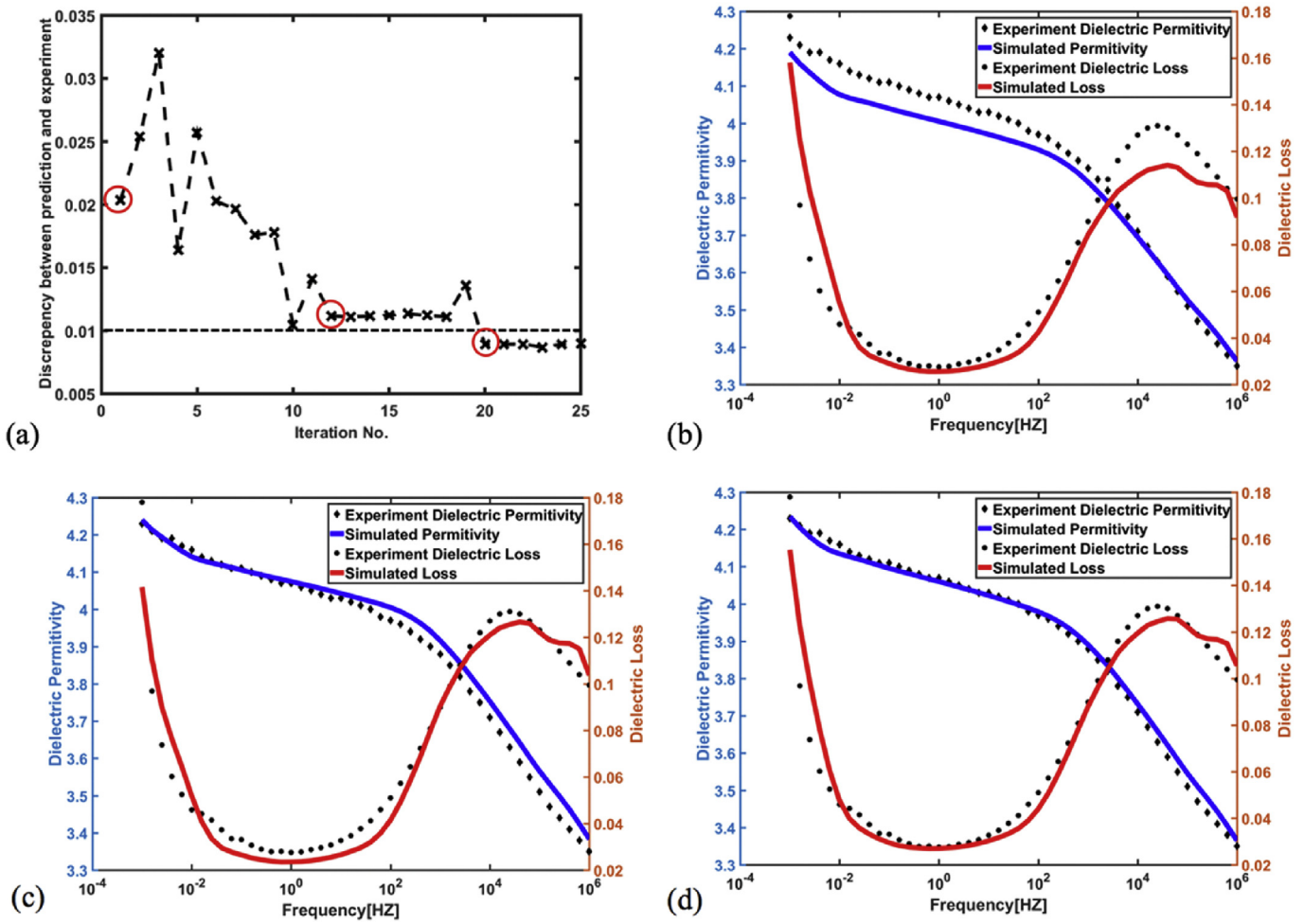

Fig. 8. Evolving of optimal solution as a function of successive iterations; (a) The discrepancy between the optimal prediction and the experimental data as a function of iterations; (b) Comparison between experimental data and the simulated result on iteration 1; (c) Comparison on iteration 12; (d) Comparison on iteration 20.

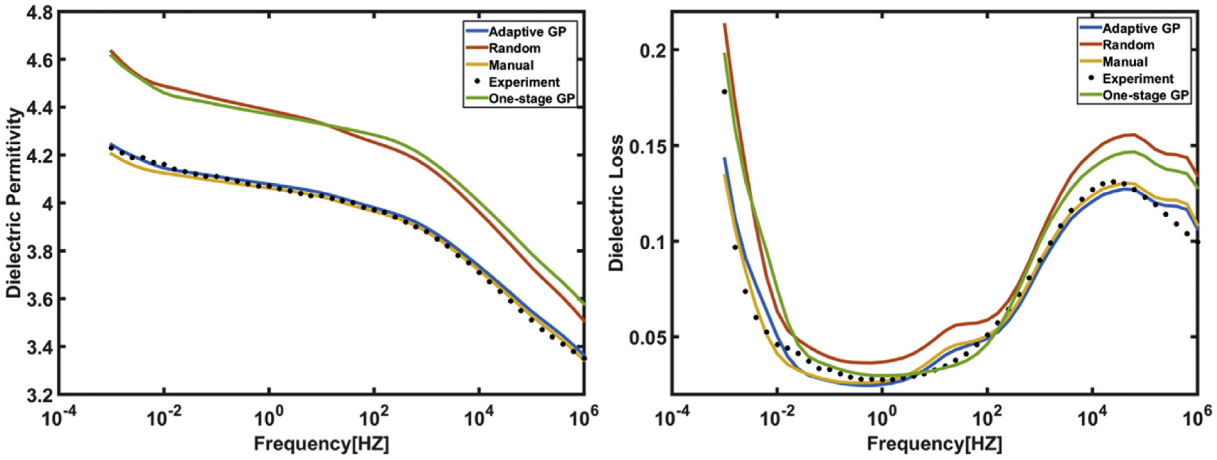

Fig. 9. Performance comparison of different searching strategies (Adaptive GP, one-stage GP, Random, Manual).

Table 2
Comparisons of different searching methods by calculating the difference.

Method	Difference between the simulation and experiment
Adaptive GP	0.0089
Manual	0.0097
One-stage GP	0.1683
Random	0.1854

and viscoelastic studies can be determined automatically. Results demonstrate that only tens of iterations are required for the method to identify the optimal shifting factors and interphase properties to achieve a good fit with the target experimental data. Comparisons are made among different searching algorithms to show the ability of our method to reduce the computational cost and improve the searching efficiency.

This method can be used as a generalized automated approach to

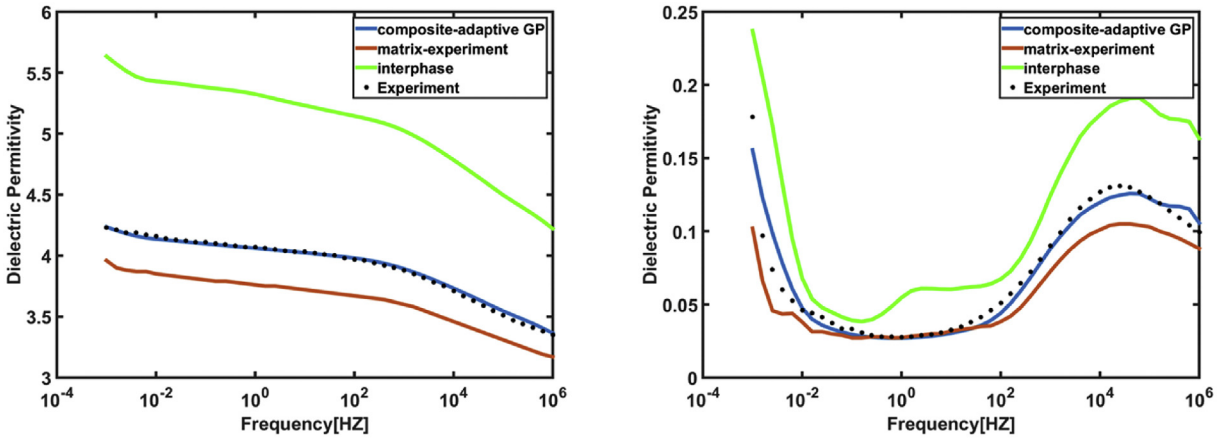

Fig. 10. Comparison between simulated dielectric spectra using the shifting factors given from adaptive GP and experimental data for 2 wt% bimodal anthracene-PGMA grafted silica in epoxy.

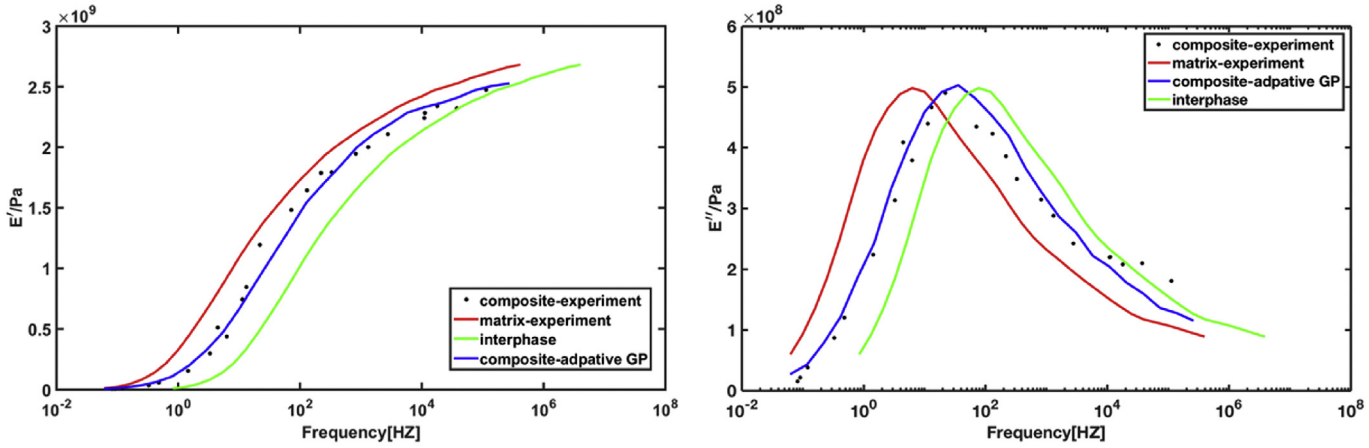

Fig. 11. Comparison between simulated viscoelastic response and experimental data for 2 wt% Chloro-modified nanosilica in PS.

determine the interphase properties in polymer nanocomposites. The framework is also flexible to be applied to other computational models to identify the interphase properties that are required. Additionally, the method is very efficient compared with the manual-fitting process and should facilitate the further investigation of a data-driven analysis where many hundreds of samples would be required. The future work may start from setting up a material interphase library through combining this method with *Nanomine*, which is a data-driven web-based platform for analysis and design of polymer nanocomposite systems under the material genome concept [57]. With sufficient data in the interphase library, relationship between the material constituents, microstructures, and the interphase properties can be created through data mining. Such relationships have the potential to improve the understanding of material principles behind interphase properties and guide the design of new materials with desired functionality and performance.

Acknowledgement

The authors would like to thank the support from CHIMAD (Center for Hierarchical Materials and Design) and NSF for this collaborative research: CHIMAD 70NANB14H012 Amd 5, NSF DEMS program CMMI-1334929 (Northwestern University) and DEMS – 000164431 (RPI) and CDMR program under grant number DMR-1310292 (Northwestern University) and CDMR - 1310318 (RPI).

Appendix A. Supplementary data

Supplementary data related to this article can be found at http://dx.doi.org/10.1016/j.compscitech.2018.04.017.

References

[1] M.B. Bryning, M.F. Islam, J.M. Kikkawa, A.G. Yodh, Very low conductivity threshold in bulk isotropic single-walled carbon nanotube–epoxy composites, Adv. Mater. 17 (9) (2005) 1186–1191.
[2] T. Kashiwagi, F. Du, J.F. Douglas, K.I. Winey, R.H. Harris, J.R. Shields, Nanoparticle networks reduce the flammability of polymer nanocomposites, Nat. Mater. 4 (12) (2005) 928–933.
[3] S. Zhang, N. Zhang, C. Huang, K. Ren, Q. Zhang, Microstructure and electromechanical properties of carbon nanotube/poly (vinylidene fluoride—trifluoroethylene—chlorofluoroethylene) composites, Adv. Mater. 17 (15) (2005) 1897–1901.
[4] M. Moradi, J.A. Mohandesi, D.F. Haghshenas, Mechanical properties of the poly (vinyl alcohol) based nanocomposites at low content of surfactant wrapped graphene sheets, Polymer 60 (2015) 207–214.
[5] S.M. Hosseini, M. Razzaghi-Kashani, Vulcanization kinetics of nano-silica filled styrene butadiene rubber, Polymer 55 (24) (2014) 6426–6434.
[6] Y. Zare, H. Garmabi, Attempts to simulate the modulus of polymer/carbon nanotube nanocomposites and future trends, Polym. Rev. 54 (3) (2014) 377–400.
[7] M. Norouzi, Y. Zare, P. Kiany, Nanoparticles as effective flame retardants for natural and synthetic textile polymers: application, mechanism, and optimization, Polym. Rev. 55 (3) (2015) 531–560.
[8] E.K. Hobbie, J.A. Fagan, J. Obrzut, S.D. Hudson, Microscale polymer − nanotube composites, ACS Appl. Mater. Interfaces 1 (7) (2009) 1561–1566.
[9] L. Xie, X. Huang, C. Wu, P. Jiang, Core-shell structured poly (methyl methacrylate)/BaTiO 3 nanocomposites prepared by in situ atom transfer radical polymerization: a route to high dielectric constant materials with the inherent low loss of the base polymer, J. Mater. Chem. 21 (16) (2011) 5897–5906.
[10] A.-L. Goffin, J.-M. Raquez, E. Duquesne, G. Siqueira, Y. Habibi, A. Dufresne,

P. Dubois, Poly (ε-caprolactone) based nanocomposites reinforced by surface-grafted cellulose nanowhiskers via extrusion processing: morphology, rheology, and thermo-mechanical properties, Polymer 52 (7) (2011) 1532–1538.
[11] H. Kim, S. Kobayashi, M.A. AbdurRahim, M.J. Zhang, A. Khusainova, M.A. Hillmyer, A.A. Abdala, C.W. Macosko, Graphene/polyethylene nanocomposites: effect of polyethylene functionalization and blending methods, Polymer 52 (8) (2011) 1837–1846.
[12] D. Ciprari, K. Jacob, R. Tannenbaum, Characterization of polymer nanocomposite interphase and its impact on mechanical properties, Macromolecules 39 (19) (2006) 6565–6573.
[13] J.S. Jang, B. Bouveret, J. Suhr, R.F. Gibson, Combined numerical/experimental investigation of particle diameter and interphase effects on coefficient of thermal expansion and young's modulus of SiO2/epoxy nanocomposites, Polym. Compos. 33 (8) (2012) 1415–1423.
[14] S. Yu, S. Yang, M. Cho, Multi-scale modeling of cross-linked epoxy nanocomposites, Polymer 50 (3) (2009) 945–952.
[15] J.-L. Tsai, S.-H. Tzeng, Characterizing mechanical properties of particulate nanocomposites using micromechanical approach, J. Compos. Mater. 42 (22) (2008) 2345–2361.
[16] S. Yang, M. Cho, Scale bridging method to characterize mechanical properties of nanoparticle/polymer nanocomposites, Appl. Phys. Lett. 93 (4) (2008) 043111.
[17] D.G. Yablon, A. Gannepalli, R. Proksch, J. Killgore, D.C. Hurley, J. Grabowski, A.H. Tsou, Quantitative viscoelastic mapping of polyolefin blends with contact resonance atomic force microscopy, Macromolecules 45 (10) (2012) 4363–4370.
[18] Y. Wang, T.H. Hahn, AFM characterization of the interfacial properties of carbon fiber reinforced polymer composites subjected to hygrothermal treatments, Compos. Sci. Technol. 67 (1) (2007) 92–101.
[19] P.F. Brune, G.S. Blackman, T. Diehl, J.S. Meth, D. Brill, Y. Tao, J. Thornton, Direct measurement of rubber interphase stiffness, Macromolecules 49 (13) (2016) 4909–4922.
[20] X. Cheng, K.W. Putz, C.D. Wood, L.C. Brinson, Characterization of local elastic modulus in confined polymer films via AFM indentation, Macromol. Rapid Commun. 36 (4) (2015) 391–397.
[21] S. Watcharotone, C.D. Wood, R. Friedrich, X. Chen, R. Qiao, K. Putz, L.C. Brinson, Interfacial and substrate effects on local elastic properties of polymers using coupled experiments and modeling of nanoindentation, Adv. Eng. Mater. 13 (5) (2011) 400–404.
[22] M. Qu, F. Deng, S.M. Kalkhoran, A. Gouldstone, A. Robisson, K.J. Van Vliet, Nanoscale visualization and multiscale mechanical implications of bound rubber interphases in rubber–carbon black nanocomposites, Soft Matter 7 (3) (2011) 1066–1077.
[23] M. Zhang, S. Askar, J.M. Torkelson, L.C. Brinson, Stiffness gradients in glassy polymer model nanocomposites: comparisons of quantitative characterization by fluorescence spectroscopy and atomic force microscopy, Macromolecules 50 (14) (2017) 5447–5458.
[24] I.M. Daniel, O. Ishai, I.M. Daniel, I. Daniel, Engineering mechanics of composite materials, Oxford university press, New York, 1994.
[25] D. Colombini, G. Merle, N. Alberola, Use of mechanical modeling to study multiphase polymeric materials, Macromolecules 34 (17) (2001) 5916–5926.
[26] H. Liu, L.C. Brinson, A hybrid numerical-analytical method for modeling the viscoelastic properties of polymer nanocomposites, J. Appl. Mech. 73 (5) (2006) 758–768.
[27] D.A. Brune, J. Bicerano, Micromechanics of nanocomposites: comparison of tensile and compressive elastic moduli, and prediction of effects of incomplete exfoliation and imperfect alignment on modulus, Polymer 43 (2) (2002) 369–387.
[28] M.D. Frogley, D. Ravich, H.D. Wagner, Mechanical properties of carbon nanoparticle-reinforced elastomers, Compos. Sci. Technol. 63 (11) (2003) 1647–1654.
[29] D. Bruggeman, Calculation of various physics constants in heterogenous substances I Dielectricity constants and conductivity of mixed bodies from isotropic substances, Ann. Phys. 24 (7) (1935) 636–664.
[30] K. Lichtenecker, Dielectric constant of natural and synthetic mixtures, Phys. Z. 27 (1926) 115.
[31] M.G. Todd, F.G. Shi, Validation of a novel dielectric constant simulation model and the determination of its physical parameters, Microelectron. J. 33 (8) (2002) 627–632.
[32] R. Qiao, L.C. Brinson, Simulation of interphase percolation and gradients in polymer nanocomposites, Compos. Sci. Technol. 69 (3) (2009) 491–499.
[33] Y. Huang, T.M. Krentz, J.K. Nelson, L.S. Schadler, Y. Li, H. Zhao, L.C. Brinson, M. Bell, B. Benicewicz, K. Wu, Prediction of interface dielectric relaxations in bimodal brush functionalized epoxy nanodielectrics by finite element analysis method, 2014 IEEE Conference on Electrical Insulation and Dielectric Phenomena (CEIDP), IEEE, 2014, pp. 748–751.
[34] P. Maity, N. Gupta, V. Parameswaran, S. Basu, On the size and dielectric properties of the interphase in epoxy-alumina nanocomposite, IEEE Trans. Dielectr. Electr. Insul. 17 (6) (2010) 1665–1675.
[35] X. Bai, M.A. Bessa, A.R. Melro, P.P. Camanho, L. Guo, W.K. Liu, High-fidelity micro-scale modeling of the thermo-visco-plastic behavior of carbon fiber polymer matrix composites, Compos. Struct. 134 (2015) 132–141.
[36] C.M. Breneman, L.C. Brinson, L.S. Schadler, B. Natarajan, M. Krein, K. Wu, L. Morkowchuk, Y. Li, H. Deng, H. Xu, Stalking the materials genome: a data-driven approach to the virtual design of nanostructured polymers, Adv. Funct. Mater. 23 (46) (2013) 5746–5752.
[37] F. Feyel, J.-L. Chaboche, FE 2 multiscale approach for modelling the elastovisco-plastic behaviour of long fibre SiC/Ti composite materials, Comput. Meth. Appl. Mech. Eng. 183 (3) (2000) 309–330.
[38] H. Deng, Y. Liu, D. Gai, D.A. Dikin, K.W. Putz, W. Chen, L.C. Brinson, C. Burkhart, M. Poldneff, B. Jiang, Utilizing real and statistically reconstructed microstructures for the viscoelastic modeling of polymer nanocomposites, Compos. Sci. Technol. 72 (14) (2012) 1725–1732.
[39] R. Qiao, H. Deng, K.W. Putz, L.C. Brinson, Effect of particle agglomeration and interphase on the glass transition temperature of polymer nanocomposites, J. Polym. Sci. B Polym. Phys. 49 (10) (2011) 740–748.
[40] C.D. Wood, A. Ajdari, C.W. Burkhart, K.W. Putz, L.C. Brinson, Understanding competing mechanisms for glass transition changes in filled elastomers, Compos. Sci. Technol. 127 (2016) 88–94.
[41] H. Zhao, Y. Li, Y. Huang, T.M. Krentz, M. Bell, B. Benicewicz, L.S. Schadler, L.C. Brinson, Dielectric Spectroscopy Analysis Using Viscoelasticity-inspired Relaxation Theory with Finite Element Modeling (accepted), IEEE Transactions on Dielectrics and Electrical Insulation, 2017.
[42] M.L. Stein, Interpolation of Spatial Data: Some Theory for Kriging, Springer Science & Business Media, 2012.
[43] Z. Qian, C.C. Seepersad, V.R. Joseph, J.K. Allen, C.J. Wu, Building surrogate models based on detailed and approximate simulations, J. Mech. Des. 128 (4) (2006) 668–677.
[44] V. Picheny, T. Wagner, D. Ginsbourger, A benchmark of kriging-based infill criteria for noisy optimization, Struct. Multidiscip. Optim. 48 (3) (2013) 607–626.
[45] W. Niblack, An Introduction to Digital Image Processing, Strandberg Publishing Company, 1985.
[46] T. Tanaka, M. Kozako, N. Fuse, Y. Ohki, Proposal of a multi-core model for polymer nanocomposite dielectrics, IEEE Trans. Dielectr. Electr. Insul. 12 (4) (2005) 669–681.
[47] D.R. Jones, M. Schonlau, W.J. Welch, Efficient global optimization of expensive black-box functions, J. Global Optim. 13 (4) (1998) 455–492.
[48] R. Jin, W. Chen, A. Sudjianto, On sequential sampling for global metamodeling in engineering design, ASME 2002 International Design Engineering Technical Conferences and Computers and Information in Engineering Conference, American Society of Mechanical Engineers, 2002, pp. 539–548.
[49] D. Xue, P.V. Balachandran, J. Hogden, J. Theiler, D. Xue, T. Lookman, Accelerated search for materials with targeted properties by adaptive design, Nat. Commun. 7 (2016).
[50] P.V. Balachandran, D. Xue, J. Theiler, J. Hogden, T. Lookman, Adaptive strategies for materials design using uncertainties, Sci. Rep. 6 (2016).
[51] S. Sakata, F. Ashida, Ns-kriging based microstructural optimization applied to minimizing stochastic variation of homogenized elasticity of fiber reinforced composites, Struct. Multidiscip. Optim. 38 (5) (2009) 443–453.
[52] S. Virtanen, T.M. Krentz, J.K. Nelson, L.S. Schadler, M. Bell, B. Benicewicz, H. Hillborg, S. Zhao, Dielectric breakdown strength of epoxy bimodal-polymer-brush-grafted core functionalized silica nanocomposites, IEEE Trans. Dielectr. Electr. Insul. 21 (2) (2014) 563–570.
[53] I. Hassinger, X. Li, H. Zhao, H. Xu, Y. Huang, A. Prasad, L. Schadler, W. Chen, L.C. Brinson, Toward the development of a quantitative tool for predicting dispersion of nanocomposites under non-equilibrium processing conditions, J. Mater. Sci. 51 (9) (2016) 4238–4249.
[54] H. Xu, Y. Li, C. Brinson, W. Chen, A descriptor-based design methodology for developing heterogeneous microstructural materials system, J. Mech. Des. 136 (5) (2014) 051007.
[55] J.-S. Park, Optimal Latin-hypercube designs for computer experiments, J. Stat. Plann. Inference 39 (1) (1994) 95–111.
[56] C.D. Wood, L. Chen, C. Burkhart, K.W. Putz, J.M. Torkelson, L.C. Brinson, Measuring interphase stiffening effects in styrene-based polymeric thin films, Polymer 75 (2015) 161–167.
[57] H. Zhao, X. Li, Y. Zhang, L.S. Schadler, W. Chen, L.C. Brinson, Perspective: NanoMine: a material genome approach for polymer nanocomposites analysis and design, Apl. Mater. 4 (5) (2016) 053204.